Joule

Article

Stable comprehensive dopants for efficient and scalable perovskite solar cells

Graphical abstract

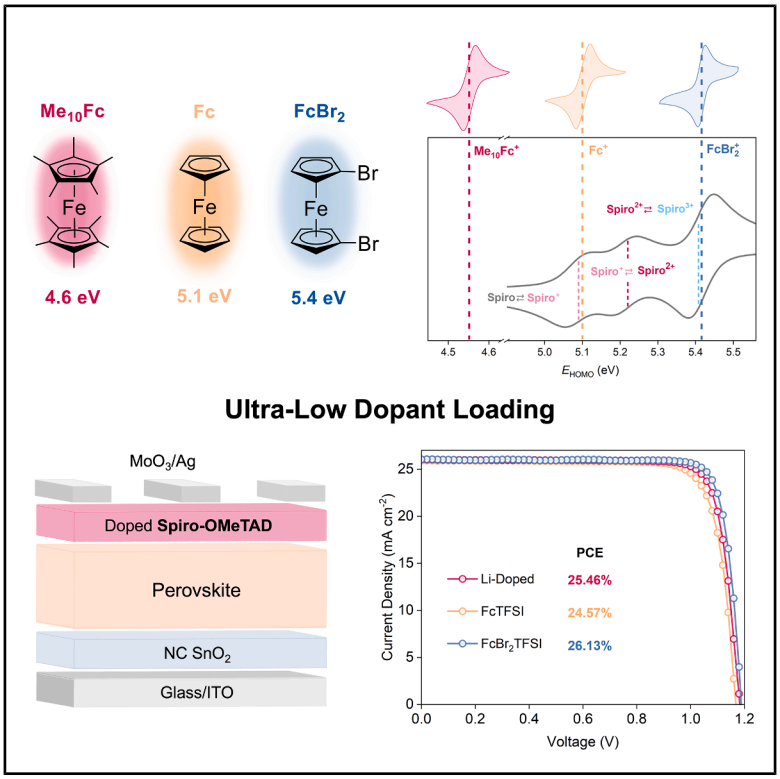

Highlights

- Introduced convenient and tunable comprehensive dopants requiring minimal loadings
- Elucidated structure-property-function and design rules for next-generation dopants
- State-of-the-art efficiency of 26.13% and 22.21% for devices and modules, respectively
- Demonstrated enhanced operational device stability, with >95% efficiency after 1,000 h

Authors

Francesco Vanin, Thomas Webb, Danpeng Gao, ..., Zonglong Zhu, Saif A. Haque, Nicholas J. Long

Correspondence

zonglzhu@cityu.edu.hk (Z.Z.), s.a.haque@imperial.ac.uk (S.A.H.), n.long@imperial.ac.uk (N.J.L.)

In brief

Despite the multitude of drawbacks discovered over the last decade, complex multicomponent Li-based doping schemes continue to dominate n-i-p perovskite solar cell applications. Herein, a single-component oxidative doping approach is demonstrated using convenient and highly tunable ferrocenium compounds. Despite the ultra-low dopant loadings, excellent device efficiency and stability are achieved, with record devices reaching power conversion efficiencies of 26.13% and maintaining >95% of their initial efficiency after 1,000 h of continuous operation.

Vanin et al., 2026, Joule *10*, 102310
March 18, 2026
https://doi.org/10.1016/j.joule.2025.102310

CellPress

Joule

CellPress
OPEN ACCESS

Article

Stable comprehensive dopants for efficient and scalable perovskite solar cells

Francesco Vanin,[1,2,5] Thomas Webb,[2,3,5] Danpeng Gao,[1,5] Katharine Welch,[2] William D.J. Tremlett,[2] Liangchen Qian,[1] Chunlei Zhang,[1] Ryan K. Brown,[2] Andrew J.P. White,[2] Nicola Gasparini,[2,3] Li Bo,[4] Zonglong Zhu,[1,*] Saif A. Haque,[2,3,*] and Nicholas J. Long[2,6,*]

[1]Department of Chemistry, City University of Hong Kong, Kowloon 999077, Hong Kong, China
[2]Department of Chemistry, Imperial College London, MSRH Building, White City Campus, London, W12 0BZ, UK
[3]Centre for Processable Electronics, Imperial College London, MSRH Building, White City Campus, London, W12 0BZ, UK
[4]School of Materials Science and Engineering, Central South University, Changsha 410083, China
[5]These authors contributed equally
[6]Lead contact
*Correspondence: zonglzhu@cityu.edu.hk (Z.Z.), s.a.haque@imperial.ac.uk (S.A.H.), n.long@imperial.ac.uk (N.J.L.)
https://doi.org/10.1016/j.joule.2025.102310

CONTEXT & SCALE Regular (n-i-p) perovskite solar cells (PSCs) featuring doped Spiro-OMeTAD hole transport materials (HTMs) have led the remarkable push for efficiency in the field over the last decade. However, the unanimous adoption of lithium-based doping schemes requiring a large excess of problematic additives (>300 mol % 4-*tert*-butyl pyridine TBP and >50 mol % lithium bis(trifluoromethylsulfonyl)imide LiTFSI), known for their hygroscopic and volatile nature, significantly limits long-term PSC stability. Therefore, developing accessible single-component dopants affording excellent PSC performance at low dopant loadings is crucial for the future of the field.

To address these challenges, we have successfully introduced a novel class of highly tunable ferrocenium dopants that afford exceptional PSC device and module performance at minimal dopant loadings (5 mol %), avoiding LiTFSI and TBP entirely. Additionally, we developed a convenient one-step glovebox synthesis from commercially available precursors. Through this approach, oxidative strength, counterion, and substitution of ferrocenium compounds can be simultaneously tuned, affording ample room for further exploration. Our work establishes design rules to break the dependence on problematic LiTFSI-based doping schemes. We expect this work to also draw interest from the broader organic semiconductor field, given the broad applications of organic semiconductor dopants.

SUMMARY

Controlled doping of organic semiconductors is crucial for their application in optoelectronic devices. In perovskite solar cells (PSCs), breakthrough efficiencies have relied on doped Spiro-OMeTAD hole transport materials. However, the ubiquitous adoption of multicomponent lithium-based doping schemes, known for their hygroscopic, volatile, and temperamental nature, remains a major issue for n-i-p PSCs. Therefore, next-generation dopants must be re-engineered from first principles. Here, we report a class of tailored ferrocenium oxidants as high-performance, comprehensive Spiro-OMeTAD dopants. Tuning ferrocenium reduction potentials enables near-quantitative Spiro-OMeTAD$^{\cdot+}$ conversion, affording optimal electronic and energetic properties. The resulting ferrocenium-doped PSCs outperform conventional counterparts, achieving device and module efficiencies of 26.13% and 22.21%, respectively, with ultra-low dopant loadings. Devices show excellent operational stability, retaining 95% (unheated) and 87% (held at 65°C) of the initial efficiency after 1,000 h of continuous operation. Our results reveal the unrecognized potential of comprehensive doping paradigms in PSCs and beyond.

INTRODUCTION

Advancements in the power conversion efficiency (PCE) of perovskite solar cells (PSCs) have been driven by regular (n-i-p) architectures utilizing a doped small molecule hole transport material (HTM), 2,2',7,7'-tetrakis[N,N-di(4-methoxyphenyl)amino]-9,9'-spirobifluorene (Spiro-OMeTAD).[1–3] Notably, despite the numerous known drawbacks, a problematic lithium-based

approach to Spiro-OMeTAD doping has come to dominate the literature.[4,5] This near-ubiquitous doping methodology involves the addition of excess lithium bis(trifluoromethylsulfonyl)imide (LiTFSI, >50 mol %) and 4-*tert*-butyl pyridine (TBP, >300 mol %), followed by several hours of dry oxygen exposure. Each component carries critical issues, including LiTFSI's hygroscopicity and diffusivity, TBP's volatility and de-doping, and the time-consuming and temperamental oxidation procedure.[6–9] Consequently, although impressive improvements in PCE have been realized, the issues relating to stability, reproducibility, and scalability associated with doping remain significant unresolved obstacles for the advancement of n-i-p PSC technologies.

Several approaches have been developed to address one or more of the abovementioned drawbacks and can broadly be categorized as O_2-free, Li-free, or comprehensive. O_2-free strategies generally introduce additional oxidizing additives to the dopant composition,[10–13] while Li-free strategies focus on alternative oxidative procedures replacing LiTFSI.[14–16] Crucially, co-doping with TBP is unanimously adopted. More recently, comprehensive doping schemes seeking to replace LiTFSI, TBP, and O_2 altogether have also appeared,[17,18] the most appealing of which achieve state-of-the-art PSC performance with small quantities of single dopants (<10 mol %).[19–22] The success of these strategies represents a paradigm shift in Spiro-OMeTAD doping that mirrors developments in the broader organic semiconductor (OS) doping literature: efficient oxidation at low dopant loadings.[22,23] Nonetheless, leading contemporary n-i-p PSCs still rely on LiTFSI, indicating that a greater focus on accessibility, convenience, reliability, and tunability is required for next-generation doping procedures to take hold.[1,24]

Aiming to address this gap in the literature, we developed a convenient one-step synthetic route to redox-tunable and anion-selective ferrocenium oxidants. The more strongly oxidizing dibromo-ferrocenium compound ($FcBr_2$TFSI) affords near-quantitative Spiro-OMeTAD$^{\cdot+}$ conversion, boosting electrical and energetic HTM properties. Additionally, time-resolved spectroscopic techniques revealed improved hole extraction rates, yields, and lifetimes at the perovskite/HTM interface. Resulting n-i-p PSCs fabricated with $FcBr_2$TFSI achieved a record Li-free PCE of 26.1% without co-dopants at minimal dopant loadings (5 mol %). By avoiding LiTFSI and TBP, devices exhibited excellent stability, maintaining 95% of their initial PCE after 1,000 h of maximum power point (MPP) operation. Owing to the rich synthetic history of ferrocene and the simple oxidative approach highlighted herein, this class of highly tunable dopants holds significant potential in PSC and broader OS doping applications.

RESULTS AND DISCUSSION

Compound selection

We began by identifying the key properties of an ideal p-type Spiro-OMeTAD dopant for n-i-p PSCs: (1) strong and tunable reduction potential (E_{Red}), (2) function without the need for co-dopants at low dopant loadings, (3) enable anion-selectivity across a library of counterions, (4) stable in oxidized and reduced forms, (5) processable in various solvents, (6) conveniently synthesized, and (7) structurally tunable. These criteria were developed following an overview of the contemporary OS doping literature focusing on the role of LiTFSI in n-i-p PSCs (Note S1).[7,25–27] Ferrocenium compounds, despite remaining largely unexplored as OS dopants, are uniquely suited to meet the above-listed criteria, as discussed point-by-point in Note S2.[28,29]

The synthetic route shown in Figure 1A is proposed to evaluate the applicability of ferrocenium compounds as HTM dopants. The well-characterized one-step oxidation of ferrocenes by Ag salts maximizes convenience and chemical accessibility, owing to the excellent reported ferrocenium yields (>85%) and the simple purification, allowing dopant synthesis to be carried out in a glovebox without specialist equipment.[28,30] Silver bis(trifluoromethylsulfonyl)imide (AgTFSI) was chosen, as TFSI anions are known to afford optimal electrical and energetic properties.[18,26]

To highlight the tunability of ferrocenium dopants, compounds varying significantly in E_{Red} were chosen.[31] As shown in Figure 1B, we identified three compounds, decamethylferrocene ($Me_{10}Fc$; E_{Red} 4.6 eV), ferrocene (Fc; E_{Red} 5.1 eV), and dibromoferrocene ($FcBr_2$; E_{Red} 5.4 eV), with E_{Red} that lie below, within, and above the first oxidation peak of Spiro-OMeTAD, respectively.[32–34] Electrochemical characterization is provided in Figure S1 and Table S1. According to the energy level alignment of the ferrocene compounds used herein with the first three Spiro-OMeTAD oxidation potentials, highlighted in Figure 1C, the mechanistic doping scheme displayed in Figure 1D is proposed. The electron-rich $Me_{10}Fc^+$ ($E_{Red}^{Me_{10}Fc} < E_{Ox^{+1}}^{Spiro}$) should not oxidize Spiro-OMeTAD. Fc^+, having near-overlapping energetics with the first oxidation peak ($E_{Red}^{Fc} \sim E_{Ox^{+1}}^{Spiro}$), should react incompletely, giving rise to an equilibrium. The electron-poor $FcBr_2^+$ ($E_{Red}^{FcBr_2} \gg E_{Ox^{+1}}^{Spiro}$), on the other hand, is expected to access all three relevant Spiro-OMeTAD oxidation states ($E_{Red}^{FcBr_2} \sim E_{Ox^{+3}}^{Spiro}$).[10,33]

One-step ferrocenium synthesis

The proposed one-step ferrocenium synthesis and subsequent HTM doping were then attempted in the simplest case, ferrocenium TFSI (FcTFSI) (Figure S2). Briefly, a chlorobenzene solution of ferrocene is reacted with solid AgTFSI, the metallic silver precipitate is filtered, and a small quantity of the obtained blue FcTFSI stock solution is added to Spiro-OMeTAD, where the distinct purple/red color change confirms its oxidation.[11]

For this one-step process to be of use, the purity obtained must approximate that of crystalline materials. We determined the overall yields and purities of FcTFSI and $FcBr_2$TFSI samples obtained following one-step and multi-step procedures in dichloromethane (DCM) and CB. DCM is the most common solvent used for ferrocenium synthesis; however, given that Spiro-OMeTAD is processed from CB, it is preferable for the oxidant to be processed in the same. Excellent yields (>80%) were afforded in all cases, with purities indistinguishable from the crystalline counterparts by elemental analysis (Tables S2–S5). The single-crystal X-ray diffraction structure of $FcBr_2$TFSI was also collected (Figure S3). Throughout the following discussion, one-step solutions will be benchmarked against these crystalline materials for completeness.

Inductively coupled plasma optical emission spectroscopy (ICP-OES) was used to quantitatively determine the concentration of Fe and Ag present at each step of the Spiro-OMeTAD

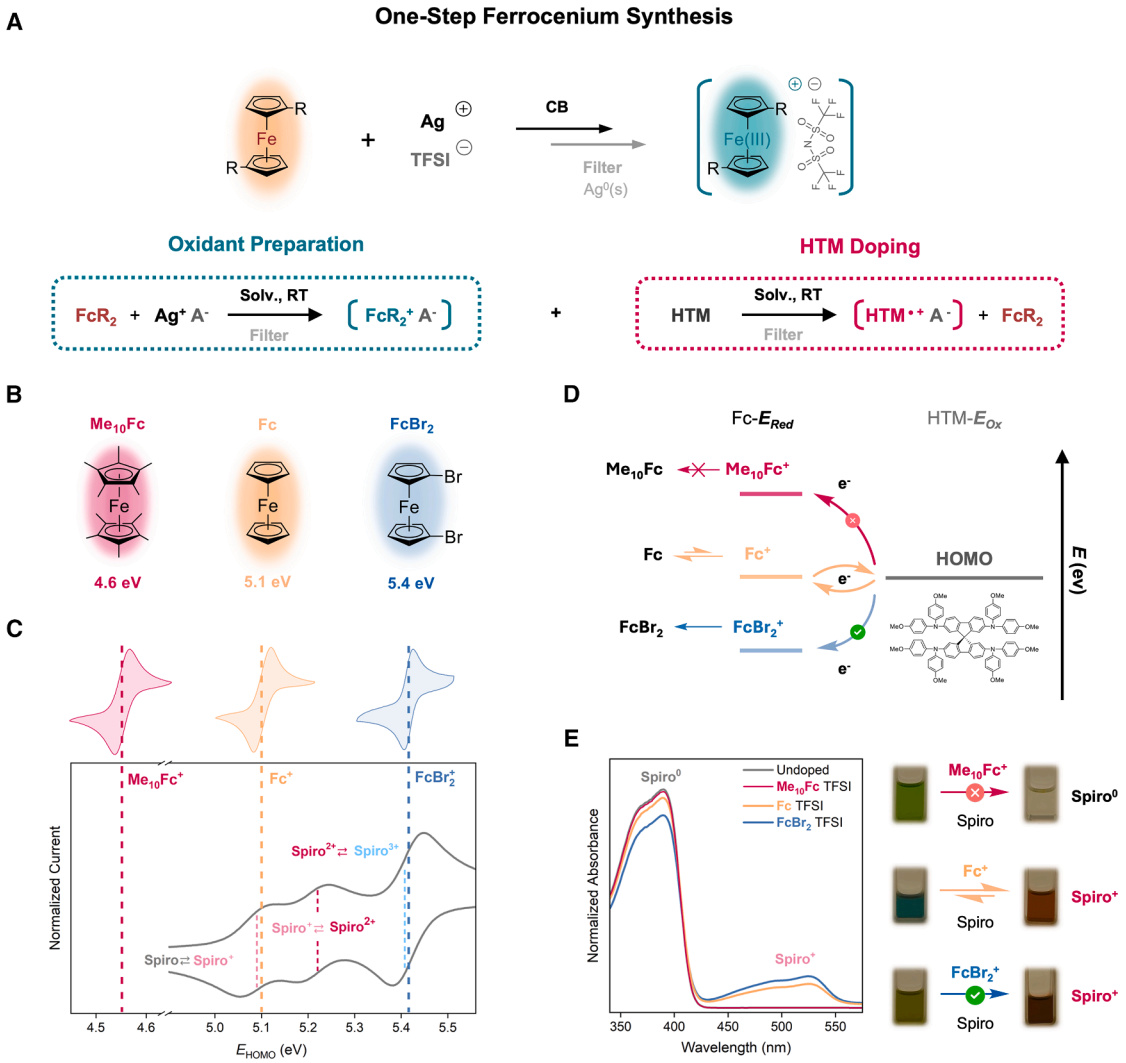

Figure 1. One-step ferrocenium synthesis and doping mechanism

(A) Proposed one-step synthesis of substituted ferrocenium $TFSI^-$ compounds and generalized HTM doping procedure, highlighting the various levels of tunability: substitution, counterion, solvent, and HTM.

(B) Chemical structure and HOMO energy determined by cyclic voltammetry of the ferrocene compounds studied herein, $Me_{10}Fc$, Fc, and $FcBr_2$.

(C) Representative alignment of the cyclic voltammograms of the chosen ferrocene compounds with Spiro-OMeTAD referenced to an internal Fc/Fc^+ redox couple translated to the vacuum scale (Fc/Fc^+ as 5.1 eV vs. vac.).

(D) Proposed E_{Red}-dependent Spiro-OMeTAD doping mechanism of ferrocenium compounds.

(E) Absorbance spectra and corresponding digital images of Spiro-OMeTAD solutions doped with 40 mol % of the respective one-step ferrocenium solutions.

HTM solution preparation (Tables S6–S8; Figure S4; Note S3). The digested precursor reagents, AgTFSI, Fc, and $FcBr_2$, showed near-quantitative recoveries with no noticeable contamination, indicating a suitable digestion procedure was developed (Table S6). Analysis of equimolar aliquots of the one-step reaction solutions revealed consistent Fe recoveries along with unexpectedly high concentrations of Ag, likely originating from small quantities of Ag powder or unreacted AgTFSI (Table S7). As unwanted Ag impurities may harm device performance, we verified whether Ag remains in the final doped HTM solution by reacting one-step solutions with pristine Spiro-OMeTAD at device-relevant concentrations. The results revealed no Ag remains (Table S8) in the final HTM solution, suggesting negligible residual contamination during device fabrication and alleviating concerns of silver impurities affecting device performance. A detailed discussion on the elemental analysis and ICP-OES results is presented in Note S4.

Elucidating the doping mechanism

Ultraviolet-visible-near-infrared (UV-vis-NIR) spectroscopy was employed to elucidate the doping mechanism of ferrocenium compounds. As shown in Figure 1E, no noticeable color change was observed when the one-step $FcMe_{10}TFSI$ solution was added to the colorless undoped spiro solution. When FcTFSI

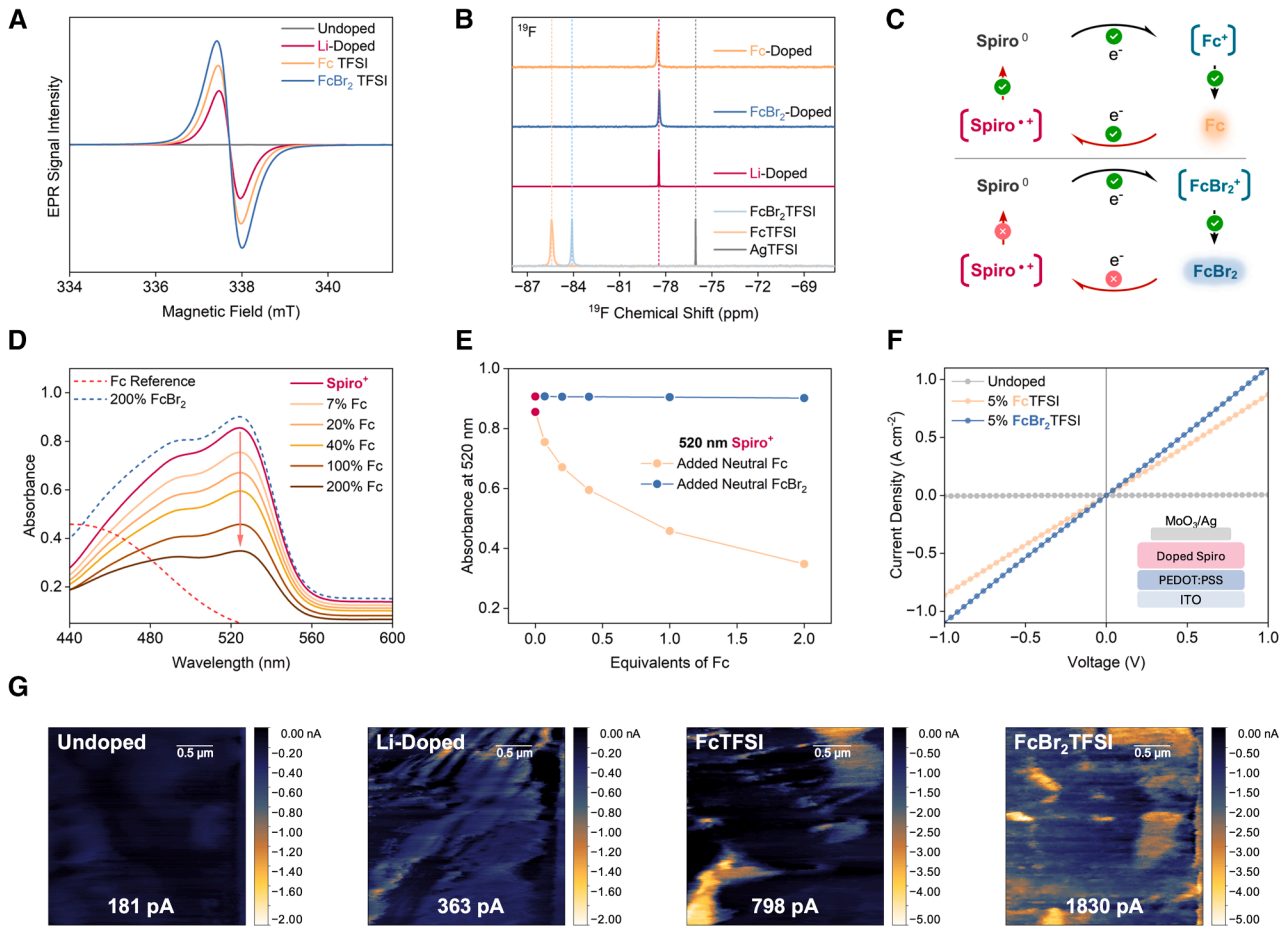

Figure 2. Properties of ferrocenium-doped Spiro-OMeTAD

(A) EPR spectra of Spiro-OMeTAD solutions doped with Li-based and 5 mol % of ferrocenium-based oxidants.

(B) ^{19}F-NMR spectra tracking the chemical environment of the $TFSI^-$ anion from ferrocenium synthesis to doped HTM.

(C) Proposed hole back transfer equilibrium reactions of Fc and $FcBr_2$ dopants expected from their respective E_{Red}.

(D) Changes in the Spiro-OMeTAD$^{\cdot+}$ absorbance spectrum following the addition of excess neutral ferrocenes.

(E) Extracted change in intensity of the 520 nm Spiro-OMeTAD$^{\cdot+}$ peak as a function of added neutral Fc and $FcBr_2$.

(F) J-V characteristics of hole-only devices with FcTFSI- and $FcBr_2$TFSI-doped Spiro-OMeTAD layers.

(G) C-AFM images of Si/perovskite/doped-HTM samples and the respective calculated average current.

was added instead, a rapid color change was observed with the concomitant appearance of a peak at 520 nm, characteristic of oxidized Spiro-OMeTAD$^{\cdot+}$, which further increased with equimolar $FcBr_2$TFSI doping.[33] To understand the role played by E_{Red} in controlling doping efficiency, the absorbance spectra of Spiro-OMeTAD sequentially doped with one-step FcTFSI and $FcBr_2$TFSI were measured (Figures S5 and S6). A lower doping efficiency of approximately 66% was obtained for FcTFSI compared with approximately 92% for $FcBr_2$TFSI, as measured from the slope of the linear increase in 520 nm absorbance (Figure S7).[35] Indeed, the more strongly oxidizing $FcBr_2$TFSI offers near-quantitative Spiro-OMeTAD$^{\cdot+}$ conversion across the whole measured range. One-step and crystalline $FcBr_2$TFSI samples afforded near-identical doping intensities (Figure S8). To evaluate the ability of $FcBr_2$TFSI to access all three of the available Spiro-OMeTAD oxidation states, full-spectrum absorption measurements at higher dopant loadings were collected (Figures S9 and S10). As expected, further addition of FcTFSI led to minimal changes in measured absorption; however, following equimolar addition of $FcBr_2$TFSI, peaks consistent with Spiro$^+$, Spiro^{2+}, and Spiro^{3+} sequentially appeared. Interestingly, the color change from purple/red to bright blue observed in $FcBr_2$TFSI samples, characteristic of highly doped Spiro-OMeTAD, could not be achieved with the popular Co(III) (FK209) p-type dopant.[10,32]

Electron paramagnetic resonance (EPR) spectroscopy was employed to quantitatively determine the free Spiro-OMeTAD$^{\cdot+}$ radical concentration afforded by conventional, FcTFSI, and $FcBr_2$TFSI doping procedures (Figure 2A).[36] Integration of the EPR signals (Figure S11; Table S9) afforded Spiro-OMeTAD$^{\cdot+}$ radical yields of 1.63, 2.95, and 4.36 % for LiTFSI, FcTFSI, and $FcBr_2$TFSI doped samples, respectively.[36] This corresponds to

doping efficiencies of 59% for FcTFSI and 87% for $FcBr_2$TFSI, in excellent agreement with absorbance measurements. Additionally, the doping efficiency obtained using one-step and crystalline $FcBr_2$TFSI was indistinguishable (Figures S12 and S13; Table S10).

High-resolution nuclear magnetic resonance (NMR) spectroscopy was employed to monitor the changes in the chemical environment of the fluorine atoms (^{19}F-NMR) of the TFSI anion through the series of reactions, starting with AgTFSI (δ −76.1 ppm), then FcTFSI (δ −85.4 ppm) and $FcBr_2$TFSI (δ −84.1 ppm), and finally to Spiro-OMeTAD$^{\cdot+}$ $TFSI^-$ (δ −78.4 ppm), as shown in Figure 2B. The difference in chemical shift between AgTFSI and the oxidized ferrocenium cations, along with the lack of residual peaks, provides additional evidence for the clean synthesis of FcTFSI and $FcBr_2$TFSI by the one-step method. The concomitant shift of the ^{1}H-NMR signals of the neutral compounds upon the addition of AgTFSI confirms the formation of paramagnetic ferrocenium cations (Figure S14).[37]

According to the scheme shown in Figure 1A, ferrocenium dopants are expected to regenerate their neutral ferrocene counterparts following oxidation of the OS host. The presence of equilibria between dopants and Spiro-OMeTAD$^{\cdot+}$ should be avoided (Figure 2C) as it may decrease doping efficiency, trap hole transport, or engender unwanted reactivity.[38] To evaluate the role of neutral ferrocenes in the doping process, absorbance measurements following the incremental addition of Fc and $FcBr_2$ to doped Spiro-OMeTAD solutions were performed (Figure 2D). A decrease in Spiro-OMeTAD$^{\cdot+}$ absorbance was observed following the sequential addition of neutral Fc; however, no such effect was noted for $FcBr_2$ (Figures 2E and S15). These results agree with the energetics of the compounds involved (Figure 1C) and the mechanistic schemes highlighted in Figures 2C and S16, indicating that negligible $FcBr_2$TFSI remains after doping and that neutral $FcBr_2$ does not negatively impact Spiro-OMeTAD$^{\cdot+}$, in contrast to Fc.

The ability of these compounds to dope other common OS is also critical to their widespread application. We therefore measured the changes in absorbance of doped poly(3-hexylthiophene-2,5-diyl) (P3HT) and poly[bis(4-phenyl)(2,4,6-trimethylphenyl)amine (PTAA) samples. Both compounds were successfully doped by FcTFSI and $FcBr_2$TFSI (Figure S17).[35] Importantly, FcTFSI showed weaker doping ability, having a small effect on the absorbance spectrum of PTAA (E_{Ox}^{PTAA} 5.14 eV)[39] and achieving incomplete oxidation of P3HT (E_{Ox}^{P3HT} 4.9 eV),[40] highlighting the importance of tuning E_{Red} for different doping applications. The one-step synthesis of FcTFSI was also attempted in different solvents to gauge the processability of ferrocenium compounds in different device architectures (Figure S18).[41]

Electrical properties

Having established a general framework for the doping mechanism of ferrocenium compounds, we then explored the electrical properties of the resulting films. Hole-only devices with a structure of ITO/PEDOT:PSS/Spiro-OMeTAD/MoO_3/Ag (PEDOT:PSS [poly[3,4-ethylenedioxythiophene] polystyrene sulfonate]) were prepared to evaluate the conductivity of FcTFSI- and $FcBr_2$TFSI-doped films. Film conductivity rapidly increased to 1.1×10^{-5} and 1.4×10^{-5} S cm^{-1} for samples doped with 10 mol % of FcTFSI and $FcBr_2$TFSI, respectively (Figure 2F).[11] Concentration-dependent conductivity measurements (Figures S19 and S20; Table S11) revealed a 100-fold conductivity enhancement at low doping densities, between 0.1 and 2 mol %, followed by saturation.[16,31]

To better characterize the electrical effects of different doping strategies at the nanoscale in device-relevant conditions, we performed conductive atomic force microscopy (C-AFM) on Si/Perovskite/Spiro-OMeTAD samples (Figures 2G and S21). In this experiment, a constant potential is applied, and the current flowthrough the sample stack is measured at the AFM tip. The uniformly low average current measured in the undoped Spiro-OMeTAD sample of 181 pA was marginally improved upon by conventional Li-doping, reaching an average current of 363 pA.[15,18] Doping with 5 mol % of either FcTFSI or $FcBr_2$TFSI, on the other hand, led to more significant enhancements in average film conductivity, reaching 798 and 1,830 pA, respectively, suggesting improved film conductivity and significantly reduced series resistance through the perovskite/HTM junction.

Energetics and charge extraction dynamics

The increased hole density generated from chemical oxidation is expected to increase the work function (WF) of the OS material (p-doping), leading to increased band bending with the intrinsic perovskite layer and enhancing charge extraction.[17] Ultraviolet photoelectron spectroscopy (UPS) was performed to evaluate the effects of different doping strategies on the WF and highest occupied molecular orbital (HOMO) energies of the resulting films (Figures 3A and S22). Conventionally doped Spiro-OMeTAD samples afforded a WF of 4.02 eV, significantly lower than FcTFSI and $FcBr_2$TFSI counterparts, which achieved WFs of 4.15 and 4.37 eV, respectively. The decrease in the WF-HOMO gap is a characteristic trait of p-type doping and suggests changes in WF were not caused by surface dipoles.[21,23] Kelvin probe force microscopy (KPFM) was then performed to confirm the WF shifts measured by UPS and obtain nanoscale insights into doped layer morphologies. A pronounced shift in contact potential difference (CPD) from −88 to 103 and 239 mV was measured in conventional, FcTFSI, and $FcBr_2$TFSI-doped samples, respectively, in excellent agreement with the UPS data (Figures 3B and S23).

Time-resolved photoluminescence (TRPL) and transient absorption spectroscopy (TAS) were performed to track the evolution of photogenerated carriers from the perovskite layer to the HTM, affording a coherent picture of interfacial charge extraction. A stark decrease in the photoluminescence lifetime of the perovskite signal was observed when doped Spiro-OMeTAD layers were coated on the perovskite absorber (Figure 3C). This is consistent with efficient charge extraction to the HTM (Table S12).[42] However, decoupling charge extraction and interfacial recombination, which both play a role in TRPL decays at the HTM interface, is difficult by TRPL alone.[43] To address this, we performed microsecond TAS experiments to track photoexcited hole extraction to the HTM (Figure 3D) through the change in Spiro-OMeTAD$^{\cdot+}$ absorbance (ΔOD) at 1,600 nm (Figure S9).[44] The initial ΔOD signal (ΔOD_{Max}) gives qualitative insight into the density of holes extracted to the HTM, while the lifetime (τ_{rec}) relates to recombination processes.

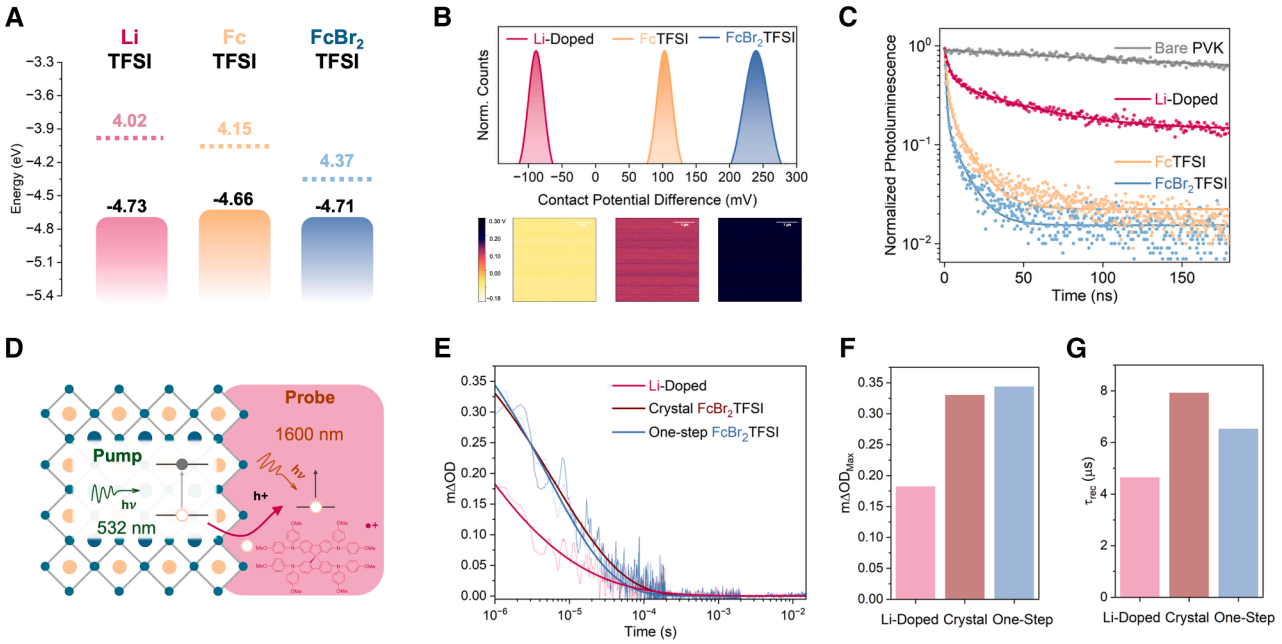

Figure 3. Energetics and interfacial charge transfer

(A) Work function and valence band energies of doped Spiro-OMeTAD layers extracted from UPS spectra.

(B) KPFM maps of doped Spiro-OMeTAD layers along with the extracted potential distributions.

(C) TRPL spectra at the perovskite/HTM interface for each doping condition fitted with biexponential decay functions.

(D) Schematic diagram detailing the TAS measurement principle.

(E) Microsecond TAS spectrum probing the Spiro-OMeTAD$^{\cdot+}$ polaron decay following perovskite photoexcitation.

(F and G) Peak hole density and polaron lifetimes extracted from the TAS spectrum.

We then compared the charge extraction profiles of one-step and crystalline $FcBr_2TFSI$ samples to Li-doped controls (Figure 3E). The ΔOD_{Max} measured at 1 μs is nearly double in the $FcBr_2TFSI$ samples than in conventionally doped samples (Figure 3F). This suggests that more holes are transferred from the perovskite absorber to Spiro-OMeTAD in the $FcBr_2TFSI$-doped systems, consistent with the decrease in the perovskite photoluminescence lifetime seen in the TRPL spectra. Despite the perovskite signal decaying on the nanosecond timescale, a significant portion of holes is still present in the Spiro-OMeTAD layer after several microseconds, with calculated recombination lifetimes of τ_{rec} of 6.5, 7.9, and 4.7 μs for one-step, crystalline, and Li-doped traces (Figure 3G), respectively. No significant difference between the two $FcBr_2TFSI$ preparation methods is noted, supporting the validity of the convenient one-step method.

Device performance

We fabricated n-i-p PSCs with a structure of ITO/SnO_2/$(FA_{0.98}MA_{0.02})_{0.95}Cs_{0.05}Pb(I_{0.98}Br_{0.02})_3$/Spiro-OMeTAD/$MoO_3$/Ag (Figures 4A and S24) to evaluate the effects of the different doping strategies on device efficiency and stability. One-step synthesized $FcBr_2TFSI$ dopants afforded the best-performing PSC devices, delivering an excellent champion PCE of 26.13% with an open circuit voltage (V_{OC}) of 1.186 V, a fill factor (FF) of 84.61%, and a short-circuit current density (J_{SC}) of 26.04 mA cm^{-2} (Figures 4B and 4C). LiTFSI- and FcTFSI-doped counterparts achieved champion PCEs of 25.46% (V_{OC} 1.182 V, FF 82.75%, J_{SC} 26.03 mA cm^{-2}) and 24.57% (V_{OC} 1.168 V, FF 81.19%, J_{SC} 25.91 mA cm^{-2}), respectively (Figure S25; Table S13). The J_{SC} values obtained from the presented J-V scans are in good agreement with the integrated external quantum efficiency (EQE) spectra in all cases (Figures 4D and S26). An optimal doping level of 5 mol % was found for the one-step process (Figure S27; Table S14). We further evaluated the stabilized power output (SPO) of the best-performing devices tracked at MPP over 300 s and measured a stabilized PCE of 25.73% at 1.04 V for the best $FcBr_2TFSI$-doped device (Figures 3E and S28). Compared with recent literature reports, one-step $FcBr_2TFSI$ dopants significantly outperformed other modified doping strategies (Figure 4E; Table S15).

Analyzing the statistical distribution of the photovoltaic parameters from 22 devices revealed that the improved PCE in $FcBr_2TFSI$-doped devices stems primarily from enhanced V_{OC} and FF values (Figure S29). Average V_{OC} and FF values rose from 1.171 V and 81.97% in Li-doped samples to 1.178 V and 83.94% in one-step $FcBr_2TFSI$ samples. We attribute this to the higher concentration of Spiro-OMeTAD$^{\cdot+}$ radicals formed using one-step $FcBr_2TFSI$ dopants, leading to increased film conductivity, improved energetic alignment, and enhanced charge extraction. Interestingly, the average FF of FcTFSI-doped samples (80.47%) fell below the Li-doped controls. We attribute this to the temporary trapping of holes via the Fc-Spiro-OMeTAD$^{\cdot+}$ equilibrium, retarding charge extraction at the

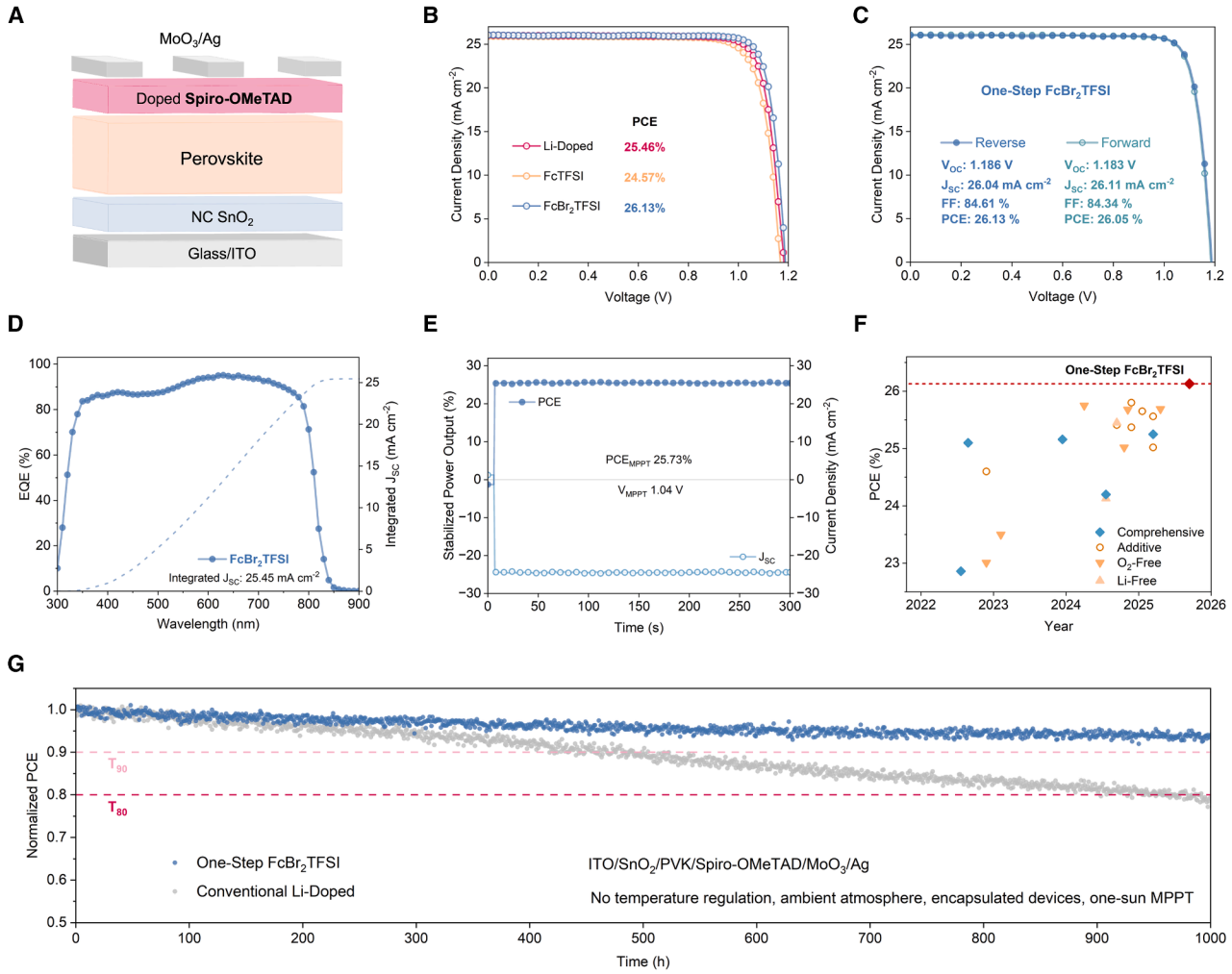

Figure 4. Device performance

(A) Schematic diagram of the n-i-p PSC structure.

(B) Reverse scan J-V curves of the best-performing control, 5 mol % FcTFSI, and 5 mol % $FcBr_2$TFSI-doped Spiro-OMeTAD layers.

(C) Forward and reverse scans of the champion 5 mol % one-step $FcBr_2$TFSI-doped device.

(D) EQE spectrum and integrated J_{SC} of the champion 5 mol % one-step $FcBr_2$TFSI-doped device.

(E) Stabilized photocurrent and corresponding PCE of the champion 5 mol % one-step $FcBr_2$TFSI-doped device operating at 1.4 V.

(F) Summary of the recently reported champion PSC PCEs featuring modified Spiro-OMeTAD doping approaches.

(G) MPPT of encapsulated Li-doped and $FcBr_2$TFSI-doped (5 mol %) PSCs over 1,000 h of continuous operation under one-sun equivalent LED illumination with no temperature control.

electrodes during device operation. We also evaluated the efficiency of crystalline $FcBr_2$TFSI-doped devices, achieving a PCE of 25.35% (V_{OC} 1.172 V, FF 83.31%, J_{SC} 25.96 mA cm^{-2}) (Figures S30 and S31). Additionally, to prove the translatability of these compounds to large-scale processing, we fabricated perovskite solar modules with an active area of 13.1 cm^2, achieving a PCE of 22.21% (V_{OC} 5.89 V, FF 76.37%, J_{SC} 4.94 mA cm^{-2}) with $FcBr_2$TFSI-doped Spiro-OMeTAD HTMs (Figures S32 and S33).

Lastly, we evaluated the long-term operational stability of encapsulated cells with LiTFSI and $FcBr_2$TFSI-doped Spiro-OMeTAD (Figures 4G and S34) under MPP tracking (MPPT). Unheated Li-doped samples degraded to 79% of their initial efficiency after 1,000 h of operation, with further degradation at elevated temperatures, retaining only 73% of the initial efficiency at 65°C. Crucially, FK209 is included in all fabricated Li-based PSCs, which is known to improve Li-doped Spiro-OMeTAD stability.[3,45] $FcBr_2$TFSI-based samples, on the other hand, showed excellent stability under both testing conditions, maintaining 95% of the initial efficiency when left unheated and 87% at 65°C. We performed additional high-temperature MPPT experiments at 85°C, where, despite both LiTFSI- and $FcBr_2$TFSI-doped devices showing considerable operational performance loss, the latter maintained a promising 65% of the initial efficiency at this challenging temperature. To better isolate the inherent stability of the doped Spiro-OMeTAD layer and

understand the effects of hygroscopic LiTFSI additives, we tracked the conductivity of unencapsulated hole-only devices stored under ambient conditions (Figure S36). A clear reduction in conductivity is observed in LiTFSI-doped devices after only 14 h of storage, with complete loss of efficiency after 48 h, as compared with only minimal degradation in $FcBr_2$TFSI-doped samples. The much-improved stability of $FcBr_2$TFSI-doped Spiro-OMeTAD layers is attributed to the low dopant loading (5 mol %) required to maximize performance, in stark contrast to the conventional hygroscopic Li-doping process (Figure S37).

Conclusion

In conclusion, we have developed a convenient one-step synthetic route to a class of highly tunable ferrocenium oxidants with optimal Spiro-OMeTAD doping properties, ultimately affording n-i-p PSCs with excellent performance at minimal dopant loadings. Our work elucidates design rules for next-generation doping procedures from first principles, offering ample room for the exploration of ferrocenium oxidants, alternative counterions, and single-component dopants more broadly. Although LiTFSI and TBP have long been considered a requirement for state-of-the-art n-i-p PSC, we have shown that minimal dopant loadings (5 mol %) of appropriately engineered oxidants can afford improved efficiency, stability, scalability, and convenience. Lastly, this work offers a promising path to the broader application of ferrocenium compounds in broader OS doping applications.

RESOURCE AVAILABILITY

Lead contact

Further information and requests for resources should be directed to and will be fulfilled by the lead contact, Nicholas J. Long (n.long@imperial.ac.uk).

Materials availability

All unique reagents generated herein are available on reasonable request from the lead contact.

Data and code availability

Single-crystal X-ray data are available free of charge from the Cambridge Crystallographic Data Centre, reference number 2468297. All data needed to evaluate the conclusions in the paper are presented in the main text and supporting materials. All other datasets are available from the corresponding author upon reasonable request. No code was generated in this study.

ACKNOWLEDGMENTS

Z.L. gratefully acknowledges funding from the Science Foundation of China (52322318), the Research Grants Council of Hong Kong Grant (N_CityU102/23, C4005-22Y, C1055-23G, 11306521, 11300124, R1001-24F, and CRS_CityU104/24), the Innovation and Technology Fund (ITS/147/22FP and MHP/079/23), the Science Technology and Innovation Committee of Shenzhen Municipality (JCYJ20220818101018038), and the National Key Research and Development Program of China (no. 2023YFB3809700). S.A.H. gratefully acknowledges funding from the Engineering and Physical Sciences Research Council (EPSRC, EP/X012344/1). T.W. thanks the Engineering and Physical Sciences Research Council (EPSRC, DTP EP/T51780X/1) for funding.

AUTHOR CONTRIBUTIONS

F.V., T.W., and D.G. contributed equally to this work. Z.Z., S.A.H., and N.J.L. conceived the idea and supervised the research. F.V. and T.W. designed the project and experiments. D.G. fabricated the perovskite devices and films. F.V., T.W., W.D.J.T., and K.W. designed, synthesized, and characterized the ferrocenium compounds. F.V., L.B., D.G., L.Q., and C.Z. conducted material characterization. T.W., K.W., W.D.J.T., A.J.P.W., and R.K.B. conducted the chemical characterization. F.V., T.W., D.G., N.G., L.B., N.J.L., S.A.H., and Z.Z. drafted and finalized the manuscript. All the authors revised the manuscript.

DECLARATION OF INTERESTS

The authors declare no other competing interests.

SUPPLEMENTAL INFORMATION

Supplemental information can be found online at https://doi.org/10.1016/j.joule.2025.102310.

Received: September 19, 2025
Revised: November 26, 2025
Accepted: December 29, 2025
Published: March 2, 2026

REFERENCES

1. Li, S., Jiang, Y., Xu, J., Wang, D., Ding, Z., Zhu, T., Chen, B., Yang, Y., Wei, M., Guo, R., et al. (2024). High-efficiency and thermally stable FACsPbI3 perovskite photovoltaics. Nature *635*, 82–88. https://doi.org/10.1038/s41586-024-08103-7.
2. Tan, S., Shih, M.-C., Lu, Y., Choi, S.-G., Dong, Y., Lee, J.-H., Yavuz, I., Larson, B.W., Park, S.Y., Kodalle, T., et al. (2025). Spontaneous formation of robust two-dimensional perovskite phases. Science *388*, 639–645. https://doi.org/10.1126/science.adr1334.
3. Yoo, J.J., Seo, G., Chua, M.R., Park, T.G., Lu, Y., Rotermund, F., Kim, Y.-K., Moon, C.S., Jeon, N.J., Correa-Baena, J.-P., et al. (2021). Efficient perovskite solar cells via improved carrier management. Nature *590*, 587–593. https://doi.org/10.1038/s41586-021-03285-w.
4. Hatamvand, M., Vivo, P., Liu, M., Tayyab, M., Dastan, D., Cai, X., Chen, M., Zhan, Y., Chen, Y., and Huang, W. (2023). The role of different dopants of Spiro-OMeTAD hole transport material on the stability of perovskite solar cells: A mini review. Vacuum *214*, 112076. https://doi.org/10.1016/j.vacuum.2023.112076.
5. Shen, Y., Deng, K., and Li, L. (2022). Spiro-OMeTAD-Based Hole Transport Layer Engineering toward Stable Perovskite Solar Cells. Small Methods *6*, e2200757. https://doi.org/10.1002/smtd.202200757.
6. Lamberti, F., Gatti, T., Cescon, E., Sorrentino, R., Rizzo, A., Menna, E., Meneghesso, G., Meneghetti, M., Petrozza, A., and Franco, L. (2019). Evidence of Spiro-OMeTAD De-doping by *tert*-Butylpyridine Additive in Hole-Transporting Layers for Perovskite Solar Cells. Chem *5*, 1806–1817. https://doi.org/10.1016/j.chempr.2019.04.003.
7. Abate, A., Leijtens, T., Pathak, S., Teuscher, J., Avolio, R., Errico, M.E., Kirkpatrik, J., Ball, J.M., Docampo, P., McPherson, I., et al. (2013). Lithium salts as "redox active" p-type dopants for organic semiconductors and their impact in solid-state dye-sensitized solar cells. Phys. Chem. Chem. Phys. *15*, 2572–2579. https://doi.org/10.1039/C2CP44397J.
8. Rombach, F.M., Haque, S.A., and Macdonald, T.J. (2021). Lessons learned from spiro-OMeTAD and PTAA in perovskite solar cells. Energy Environ. Sci. *14*, 5161–5190. https://doi.org/10.1039/D1EE02095A.
9. Wang, S., Yuan, W., and Meng, Y.S. (2015). Spectrum-Dependent Spiro-OMeTAD Oxidization Mechanism in Perovskite Solar Cells. ACS Appl. Mater. Interfaces *7*, 24791–24798. https://doi.org/10.1021/acsami.5b07703.
10. Burschka, J., Kessler, F., Nazeeruddin, M.K., and Grätzel, M. (2013). Co(III) Complexes as p-Dopants in Solid-State Dye-Sensitized Solar Cells. Chem. Mater. *25*, 2986–2990. https://doi.org/10.1021/cm400796u.

11. You, S., Zeng, H., Liu, Y., Han, B., Li, M., Li, L., Zheng, X., Guo, R., Luo, L., Li, Z., et al. (2023). Radical polymeric p-doping and grain modulation for stable, efficient perovskite solar modules. Science *379*, 288–294. https://doi.org/10.1126/science.add8786.

12. Kong, J., Shin, Y., Röhr, J.A., Wang, H., Meng, J., Wu, Y., Katzenberg, A., Kim, G., Kim, D.Y., Li, T.-D., et al. (2021). CO2 doping of organic interlayers for perovskite solar cells. Nature *594*, 51–56. https://doi.org/10.1038/s41586-021-03518-y.

13. Liu, X., Zheng, B., Shi, L., Zhou, S., Xu, J., Liu, Z., Yun, J.S., Choi, E., Zhang, M., Lv, Y., et al. (2023). Perovskite solar cells based on spiro-OMeTAD stabilized with an alkylthiol additive. Nat. Photon. *17*, 96–105. https://doi.org/10.1038/s41566-022-01111-x.

14. Saygili, Y., Kim, H.-S., Yang, B., Suo, J., Muñoz-Garcia, A.B., Pavone, M., and Hagfeldt, A. (2020). Revealing the Mechanism of Doping of spiro-MeOTAD via Zn Complexation in the Absence of Oxygen and Light. ACS Energy Lett. *5*, 1271–1277. https://doi.org/10.1021/acsenergylett.0c00319.

15. Kim, S.-G., Fish, G.C., Socie, E., Terpstra, A.T., Park, D.-A., Zhu, K., Grätzel, M., Moser, J.-E., and Park, N.-G. (2024). Photo-doping of spiro-OMeTAD for highly stable and efficient perovskite solar cells. Joule *8*, 1707–1722. https://doi.org/10.1016/j.joule.2024.03.012.

16. Ye, L., Wu, J., Catalán-Gómez, S., Yuan, L., Sun, R., Chen, R., Liu, Z., Ulloa, J.M., Hierro, A., Guo, P., et al. (2024). Superoxide radical derived metal-free spiro-OMeTAD for highly stable perovskite solar cells. Nat. Commun. *15*, 7889. https://doi.org/10.1038/s41467-024-52199-4.

17. Zhang, T., Wang, F., Kim, H.-B., Choi, I.-W., Wang, C., Cho, E., Konefal, R., Puttisong, Y., Terado, K., Kobera, L., et al. (2022). Ion-modulated radical doping of spiro-OMeTAD for more efficient and stable perovskite solar cells. Science *377*, 495–501. https://doi.org/10.1126/science.abo2757.

18. Wang, T., Zhang, Y., Kong, W., Qiao, L., Peng, B., Shen, Z., Han, Q., Chen, H., Yuan, Z., Zheng, R., et al. (2022). Transporting holes stably under iodide invasion in efficient perovskite solar cells. Science *377*, 1227–1232. https://doi.org/10.1126/science.abq6235.

19. Grotevent, M.J., Lu, Y., Šverko, T., Shih, M.-C., Tan, S., Zhu, H., Dang, T., Mwaura, J.K., Swartwout, R., Beiglböck, F., et al. (2024). Additive-Free Oxidized Spiro-MeOTAD Hole Transport Layer Significantly Improves Thermal Solar Cell Stability. Adv. Energy Mater. *14*, 2400456. https://doi.org/10.1002/aenm.202400456.

20. Yang, H., Xu, T., Chen, W., Wu, Y., Guo, X., Shen, Y., Ding, C., Chen, X., Chen, H., Ding, J., et al. (2024). Iodonium Initiators: Paving the Air-free Oxidation of Spiro-OMeTAD for Efficient and Stable Perovskite Solar Cells. Angew. Chem. Int. Ed. *63*, e202316183. https://doi.org/10.1002/anie.202316183.

21. Xia, J., Zhang, Y., Xiao, C., Brooks, K.G., Chen, M., Luo, J., Yang, H., Klipfel, N.I.D., Zou, J., Shi, Y., et al. (2022). Tailoring electric dipole of hole-transporting material p-dopants for perovskite solar cells. Joule *6*, 1689–1709. https://doi.org/10.1016/j.joule.2022.05.012.

22. Luo, X., Gao, D., Zhang, D., Zhou, G., Guo, Y., Zhang, C., Zhu, Z., and Xu, B. (2025). Highly Soluble and Oxidizing Organic Salts Doped Hole-Transporting Layer Enables Efficient and Stable Perovskite Solar Cells. Adv. Funct. Mater. *35*, 2425038. https://doi.org/10.1002/adfm.202425038.

23. Scaccabarozzi, A.D., Basu, A., Aniés, F., Liu, J., Zapata-Arteaga, O., Warren, R., Firdaus, Y., Nugraha, M.I., Lin, Y., Campoy-Quiles, M., et al. (2022). Doping Approaches for Organic Semiconductors. Chem. Rev. *122*, 4420–4492. https://doi.org/10.1021/acs.chemrev.1c00581.

24. Wang, H., Su, S., Chen, Y., Ren, M., Wang, S., Wang, Y., Zhu, C., Miao, Y., Ouyang, C., and Zhao, Y. (2024). Impurity-healing interface engineering for efficient perovskite submodules. Nature *634*, 1091–1095. https://doi.org/10.1038/s41586-024-08073-w.

25. Salzmann, I., Heimel, G., Oehzelt, M., Winkler, S., and Koch, N. (2016). Molecular Electrical Doping of Organic Semiconductors: Fundamental Mechanisms and Emerging Dopant Design Rules. Acc. Chem. Res. *49*, 370–378. https://doi.org/10.1021/acs.accounts.5b00438.

26. Jacobs, I.E., Lin, Y., Huang, Y., Ren, X., Simatos, D., Chen, C., Tjhe, D., Statz, M., Lai, L., Finn, P.A., et al. (2022). High-Efficiency Ion-Exchange Doping of Conducting Polymers. Adv. Mater. *34*, e2102988. https://doi.org/10.1002/adma.202102988.

27. Yamashita, Y., Tsurumi, J., Ohno, M., Fujimoto, R., Kumagai, S., Kurosawa, T., Okamoto, T., Takeya, J., and Watanabe, S. (2019). Efficient molecular doping of polymeric semiconductors driven by anion exchange. Nature *572*, 634–638. https://doi.org/10.1038/s41586-019-1504-9.

28. Connelly, N.G., and Geiger, W.E. (1996). Chemical Redox Agents for Organometallic Chemistry. Chem. Rev. *96*, 877–910. https://doi.org/10.1021/cr940053x.

29. Khobragade, D.A., Mahamulkar, S.G., Pospíšil, L., Císařová, I., Rulíšek, L., and Jahn, U. (2012). Acceptor-Substituted Ferrocenium Salts as Strong, Single-Electron Oxidants: Synthesis, Electrochemistry, Theoretical Investigations, and Initial Synthetic Application. Chem. Eur. J. *18*, 12267–12277. https://doi.org/10.1002/chem.201201499.

30. Khan, F.S.T., Waldbusser, A.L., Carrasco, M.C., Pourhadi, H., and Hematian, S. (2021). Synthetic, spectroscopic, structural, and electrochemical investigations of ferricenium derivatives with weakly coordinating anions: ion pairing, substituent, and solvent effects. Dalton Trans. *50*, 7433–7455. https://doi.org/10.1039/D1DT01192H.

31. Pan, J., Wang, J., Li, K., Dai, X., Li, Q., Chong, D., Chen, B., Yan, J., and Wang, H. (2024). Efficient molecular doping of polymeric semiconductors improved by coupled reaction. Nat. Commun. *15*, 5854. https://doi.org/10.1038/s41467-024-50293-1.

32. Vanin, F., Tremlett, W.D.J., Gao, D., Liu, Q., Li, B., Li, S., Gong, J., Wu, X., Li, Z., Brown, R.K., et al. (2025). Modulating Perovskite Surface Energetics Through Tuneable Ferrocene Interlayers for High-Performance Perovskite Solar Cells. Angew. Chem. Int. Ed. *64*, e202424041. https://doi.org/10.1002/anie.202424041.

33. Szabó, G., and Kamat, P.V. (2025). Spiro-OMeTAD: Unique Redox Chemistry Driving The Hole Transport. ACS Energy Lett. *10*, 330–336. https://doi.org/10.1021/acsenergylett.4c03121.

34. Zhang, W., Wang, L., Guo, Y., Zhang, B., Leandri, V., Xu, B., Li, Z., Gardner, J.M., Sun, L., and Kloo, L. (2020). Single crystal structure and optoelectronic properties of oxidized Spiro-OMeTAD. Chem. Commun. (Camb) *56*, 1589–1592. https://doi.org/10.1039/C9CC09270F.

35. Sakai, N., Warren, R., Zhang, F., Nayak, S., Liu, J., Kesava, S.V., Lin, Y.-H., Biswal, H.S., Lin, X., Grovenor, C., et al. (2021). Adduct-based p-doping of organic semiconductors. Nat. Mater. *20*, 1248–1254. https://doi.org/10.1038/s41563-021-00980-x.

36. Seif-Eddine, M., Cobb, S.J., Dang, Y., Abdiaziz, K., Bajada, M.A., Reisner, E., and Roessler, M.M. (2024). Operando film-electrochemical EPR spectroscopy tracks radical intermediates in surface-immobilized catalysts. Nat. Chem. *16*, 1015–1023. https://doi.org/10.1038/s41557-024-01450-y.

37. Bluemel, J., Hebendanz, N., Hudeczek, P., Koehler, F.H., and Strauss, W. (1992). Synthesis and NMR spectroscopy of metallocenium ions. Support for a new ferromagnetic coupling mechanism in decamethylmetallocenium tetracyanoethenides. J. Am. Chem. Soc. *114*, 4223–4230. https://doi.org/10.1021/ja00037a028.

38. Hurvois, J.P., and Moinet, C. (2005). Reactivity of ferrocenium cations with molecular oxygen in polar organic solvents: Decomposition, redox reactions and stabilization. J. Organomet. Chem. *690*, 1829–1839. https://doi.org/10.1016/j.jorganchem.2005.02.009.

39. de Alencar, D.A.M., Koch, G., De Rossi, F., Generosi, A., Ferraro, G., Bonomo, M., Noola, S., Pellis, G., Quagliotto, P., Paci, B., et al. (2025). Phenothiazine-Modified PTAA Hole Transporting Materials for Flexible Perovskite Solar Cells: A Trade-Off Between Performance and Sustainability. Adv. Sustain. Syst. *9*, 2400674. https://doi.org/10.1002/adsu.202400674.

40. Liang, Z., Cheng, X., Jiang, Y., Yu, J., Xu, X., Peng, Z., Bu, L., Zhang, Y., Tang, Z., Li, M., et al. (2021). P3HT-Based Organic Solar Cells with a Photoresponse to 1000 nm Enabled by Narrow Band Gap Nonfullerene

Acceptors with High HOMO Levels. ACS Appl. Mater. Interfaces *13*, 61487–61495. https://doi.org/10.1021/acsami.1c21089.

41. Luo, J., Liu, B., Yin, H., Zhou, X., Wu, M., Shi, H., Zhang, J., Elia, J., Zhang, K., Wu, J., et al. (2024). Polymer-acid-metal quasi-ohmic contact for stable perovskite solar cells beyond a 20,000-hour extrapolated lifetime. Nat. Commun. *15*, 2002. https://doi.org/10.1038/s41467-024-46145-7.
42. Kirchartz, T., Márquez, J.A., Stolterfoht, M., and Unold, T. (2020). Photoluminescence-Based Characterization of Halide Perovskites for Photovoltaics. Adv. Energy Mater. *10*, 1904134. https://doi.org/10.1002/aenm.201904134.
43. Butler-Caddle, E., Jayawardena, K.D.G.I., Wijesekara, A., Milot, R.L., and Lloyd-Hughes, J. (2024). Distinguishing carrier transport and interfacial recombination at perovskite/transport-layer interfaces using ultrafast spectroscopy and numerical simulation. Phys. Rev. Appl. *22*, 024013. https://doi.org/10.1103/PhysRevApplied.22.024013.
44. Webb, T., Liu, X., Westbrook, R.J.E., Kern, S., Sajjad, M.T., Jenatsch, S., Jayawardena, K.D.G.I., Perera, W.H.K., Marko, I.P., Sathasivam, S., et al. (2022). A Multifaceted Ferrocene Interlayer for Highly Stable and Efficient Lithium Doped Spiro-OMeTAD-based Perovskite Solar Cells. Adv. Energy Mater. *12*, 2200666. https://doi.org/10.1002/aenm.202200666.
45. Zhu, G., Yang, L., Zhang, C., Du, G., Fan, N., Luo, Z., Zhang, X., and Zhang, J. (2022). Unveiling the Critical Role of Oxidants and Additives in Doped Spiro-OMeTAD toward Stable and Efficient Perovskite Solar Cells. ACS Appl. Energy Mater. *5*, 3595–3604. https://doi.org/10.1021/acsaem.1c04097.